inorganics

MDPI

Article

$BaTiO_3/Ni_xZn_{1-x}Fe_2O_4$ (x = 0, 0.5, 1) Composites Synthesized by Thermal Decomposition: Magnetic, Dielectric and Ferroelectric Properties

Marija Šuljagić [1], Ivan Petronijević [2], Miljana M. Mirković [3], Aleksandar Kremenović [4], Adis Džunuzović [5], Vladimir B. Pavlović [6], Aleksandra Kalezić-Glišović [7] and Ljubica Andjelković [1,*]

1 Department of Chemistry, University of Belgrade-Institute of Chemistry, Technology and Metallurgy, Njegoševa 12, 11000 Belgrade, Serbia
2 Faculty of Physics, University of Belgrade, Studentski Trg 12-16, 11000 Belgrade, Serbia
3 Department of Materials, "Vinča" Institute of Nuclear Sciences—National Institute of the Republic of Serbia, University of Belgrade, 11000 Belgrade, Serbia
4 Faculty of Mining and Geology, University of Belgrade, Djušina 7, 11000 Belgrade, Serbia
5 Institute for Multidisciplinary Research, University of Belgrade, Volgina 15, 11000 Belgrade, Serbia
6 Faculty of Agriculture, University of Belgrade, Nemanjina 6, Zemun, 11000 Belgrade, Serbia
7 Section for Amorphous Materials, Joint Laboratory for Advanced Materials of SASA, Faculty of Technical Sciences Čačak, University of Kragujevac, Svetog Save 65, 32000 Čačak, Serbia
* Correspondence: ljubica@chem.bg.ac.rs

Abstract: To investigate the influence of spinel structure and sintering temperature on the functional properties of $BaTiO_3/Ni_xZn_{1-x}Fe_2O_4$ (x = 0, 0.5, 1), $NiFe_2O_4$, $ZnFe_2O_4$, and $Ni_{0.5}Zn_{0.5}Fe_2O_4$ were in situ prepared by thermal decomposition onto $BaTiO_3$ surface from acetylacetonate precursors. As-prepared powders were additionally sintered at 1150 °C and 1300 °C. X-ray powder diffraction (XRPD) and scanning electron microscopy (SEM) coupled with electron dispersive spectroscopy (EDS) were used for the detailed examination of phase composition and morphology. The magnetic, dielectric, and ferroelectric properties were investigated. The optimal phase composition in the $BaTiO_3/NiFe_2O_4$ composite, sintered at 1150 °C, resulted in a wide frequency range stability. Additionally, particular phase composition indicates favorable properties such as low conductivity and ideal-like hysteresis loop behavior. The favorable properties of $BaTiO_3/NiFe_2O_4$ make this particular composite an ideal material choice for further studies on applications of multi-ferroic devices.

Keywords: ferroelectric; dielectric properties; magnetic properties; titanate/ferrite composites; phase composition

check for updates

Citation: Šuljagić, M.; Petronijević, I.; Mirković, M.M.; Kremenović, A.; Džunuzović, A.; Pavlović, V.B.; Kalezić-Glišović, A.; Andjelković, L. $BaTiO_3/Ni_xZn_{1-x}Fe_2O_4$ (x = 0, 0.5, 1) Composites Synthesized by Thermal Decomposition: Magnetic, Dielectric and Ferroelectric Properties. *Inorganics* **2023**, *11*, 51. https://doi.org/10.3390/inorganics11020051

Academic Editor: Torben R. Jensen

Received: 22 December 2022
Revised: 13 January 2023
Accepted: 16 January 2023
Published: 19 January 2023

1. Introduction

In the last century, a sporadic interest in multiferroism was strongly influenced by a scarcity of materials [1,2]. The discovery of extreme electric polarization behavior in $BiFeO_3$ and manganite multiferroic derivatives have accelerated research on this topic in the past two decades [3,4]. In the past few years, researchers have begun performing in-depth studies on magnetoelectric multiferroics. which are materials that display ferromagnetism and ferroelectricity simultaneously [5–9]. The perovskite compounds are one of the most promising types of magnetoelectric multiferroics [10–14]. The advantages of these novel materials can support the development of advanced devices and technologies [15–20].

There are only a few known multiferroic materials that combine the mutually exclusive functionalities of ferromagnetism and ferroelectricity in the same phase, specifically at approximately room temperature [16]. To overcome the rareness and shortcomings of single-phase magnetoelectrics, the scientific community has been focused on the development of advanced multifunctional composite materials. More specifically, the magnetoelectric coupling is a consequence of the strain induced on the interface between two different

phases [21–27]. Such heterostructured materials can satisfy technological requirements by varying the microstructure of their constituents, their volume fraction, and/or the phase composition [28,29].

Barium titanate ($BaTiO_3$) is a well-known compound used to develop magnetoelectric multiferroic materials. This is due to its unique dielectric properties in the tetragonal phase with the *P4mm* space group [30–33]. In order to design novel multiferroic composites based on barium titanate, ferrites are one of the ideal candidates due to their attractive magnetic properties [25,30,31,33–38]. Sintering is a required process for synthesis which primarily assures better mechanical coupling between ferrite and ferroelectric grains, while also promoting more pronounced magnetoelectric signals [39]. However, high sintering temperatures may lead to the formation of Fe^{2+} ions in such composites, which can cause interphase reactions and decrease electric resistivity, thus lowering the magnetoelectric response [40].

Among many spinel oxides, nickel ferrite ($NiFe_2O_4$) with an inverse spinel structure and soft magnetic nature, zinc ferrite ($ZnFe_2O_4$) with ferrimagnetic behavior in the nanometric range, alongside with mixed nickel zinc ferrites, stand out because their coercivity, electrical conductivity, and saturation magnetization can be easily tuned to address the competing demands for specific multiferroic applications [35,41,42].

Although the increase in spinel content negatively affects magnetoelectric response [40], careful selection of ferrite chemical composition, as well as an attentive choice of synthesis protocol may serve to overcome such negative influence [43–45]. Many different methods were developed for the synthesis of nanocrystalline nickel- and zinc ferrites with tailored characteristics [46–51]. The thermal decomposition of coordination compounds with simple organic ligands emerged as a method of choice due to the low reaction temperatures [52–58]. Metal carbonyls, metal carboxylates, and metal acetylacetonates were recognized as precursors to fabricate nanostructured magnetic oxides with uniform and narrow size distribution of nanoparticles, due to their high purity and cheap production [59–65].

This paper addresses a simple route to prepare a series of a composite of $BaTiO_3/Ni_xZn_{1-x}Fe_2O_4$ (x = 0, 0.5, 1) via the thermal decomposition of acetylacetonate complex precursors onto $BaTiO_3$ surface and processing of obtained structures into dense ceramics. The effect of structural properties and phase composition, as well as two sintering schedules on dielectric and ferroelectric properties of synthesized ceramic composites, was studied and explained in detail.

2. Results and Discussion

The XRPD patterns for as-prepared and sintered titanate/ferrite structures are shown in Figure 1. With the increase in sintering temperature, better crystallinity was obtained, irrespective of the investigated powder. Furthermore, peaks intensity belonging to barioferrite-like phases indicated the more intensive reaction between spinel and $BaTiO_3$ at 1300 °C. The phase composition for each investigated powder is given in Table 1. The presence of spinel and tetragonal $BaTiO_3$ phases can be clearly seen for as-prepared samples. The zinc oxide (ZnO) phase is also evident in the case of $BaTiO_3/ZnFe_2O_4$ while for the $BaTiO_3/Ni_{0.5}Zn_{0.5}Fe_2O_4$, barioferrite-like phase was formed during the thermal decomposition process. In the case of sintered samples, different barioferrite-like phases were formed. However, spinel and tetragonal $BaTiO_3$ phases remain unchanged. The transformation of $BaTiO_3$ from *P4mm* to *P4/mmm* space group was observed at 1300 °C in all studied cases.

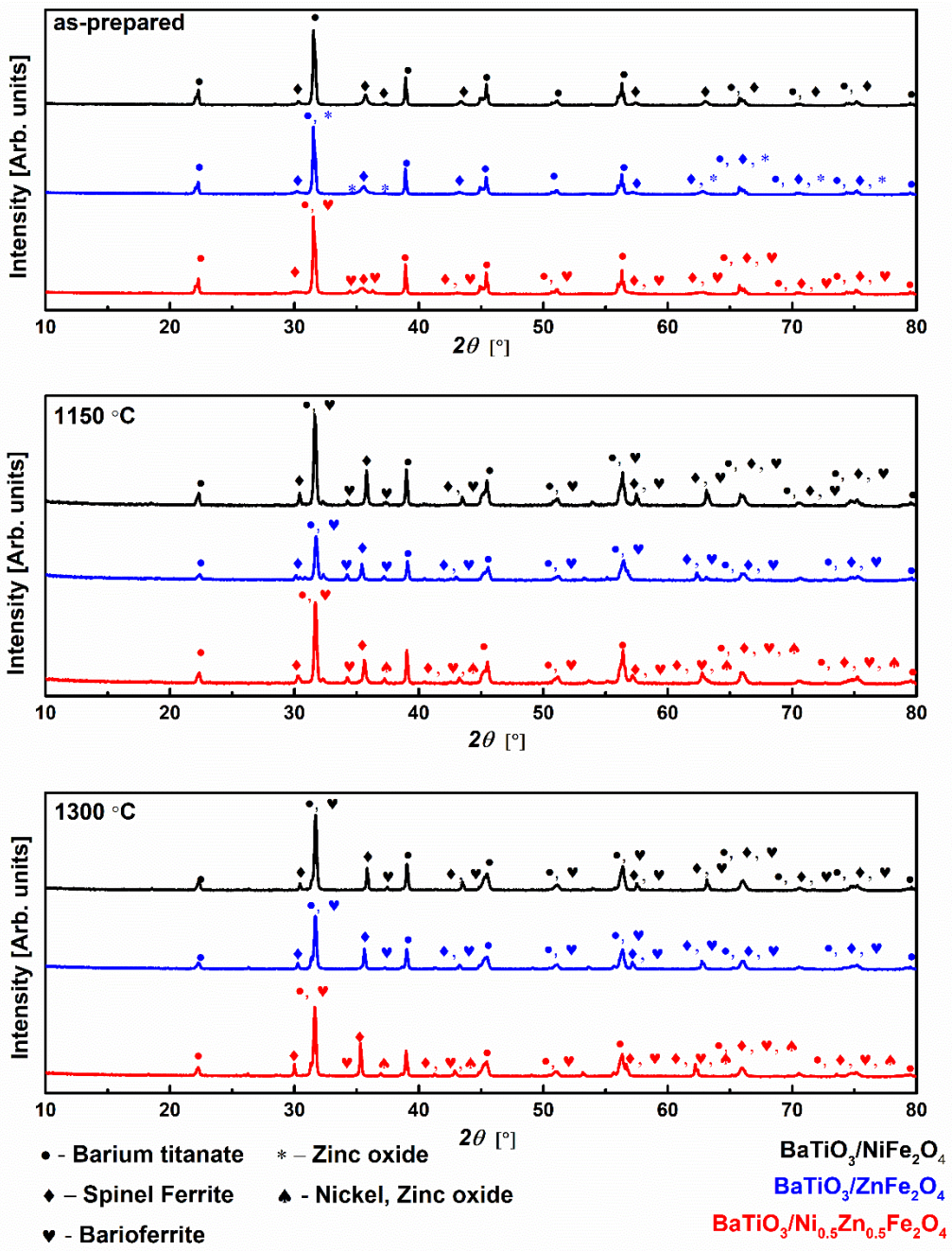

Figure 1. XRPD of $BaTiO_3/NiFe_2O_4$, $BaTiO_3/ZnFe_2O_4$, and $BaTiO_3/Ni_{0.5}Zn_{0.5}Fe_2O_4$ samples.

Table 1. The phase composition of prepared composites. In parenthesis next to the phase chemical formulae crystal system and space group are presented as well as corresponding PDF card numbers from the ICDD database. Phase abundances are calculated by the RIR method.

Samples	Phase		
$BaTiO_3/NiFe_2O_4$ as-prepared	$BaTiO_3$ Tetragonal (*P4mm*) PDF # 01-078-2738 57(2)%	$Ni_{1.3}Fe_{1.7}O_4$ Spinel (*Fd-3m*) PDF # 01-080-0072 43(2)%	/
$BaTiO_3/ZnFe_2O_4$ as-prepared	$BaTiO_3$ Tetragonal (*P4mm*) PDF # 01-081-8524 66.3(6)%	$ZnFe_2O_4$ Spinel (*Fd-3m*) PDF # 01-083-442 29.4(5)%	ZnO Wurtzite ($P6_3mc$) PDF # 01-070-8070 4.3(2)%

Table 1. *Cont.*

Samples	Phase		
$BaTiO_3/Ni_{0.5}Zn_{0.5}Fe_2O_4$ as-prepared	$BaTiO_3$ Tetragonal (*P4mm*) PDF # 01-083-8300 60(1)%	$Ni_xZn_{1-x}Fe_2O_4$ Spinel (*Fd-3m*) PDF # 01-080-4511 40(1)%	$BaTiNiFe_{10}O_{19}$ (*P6$_3$/mmc*) PDF # 00-054-0776 >1%
$BaTiO_3/NiFe_2O_4$ 1150 °C	$BaTiO_3$ Tetragonal (*P4mm*) PDF # 01-083-8300 77(2)%	$Ni_{1.25}Fe_{1.85}O_4$ Spinel (*Fd-3m*) PDF # 01-088-0380 19(2)%	$BaFe_{11.9}O_{19}$/ $BaTiNiFe_{10}O_{19}$ PDF # 01-079-1742/00-054-0776 (*P6$_3$/mmc*) 4(1)%
$BaTiO_3/ZnFe_2O_4$ 1150 °C	$BaTiO_3$ Tetragonal (*P4mm*) PDF # 00-005-0626 50(5)%	$ZnFe_2O_4$ Spinel (*Fd-3m*) PDF # 01-078-5429 46(4)%	$BaTi_{0.636}Fe_{0.364}O_{2.804}$ PDF # 01-089-4607 4(1)% $BaTiZnFe_{10}O_{19}$ PDF # 00-054-1246 >1%
$BaTiO_3/Ni_{0.5}Zn_{0.5}Fe_2O_4$ 1150 °C	$BaTiO_3$ Tetragonal (*P4mm*) PDF # 01-074-4540 40(1)%	$Ni_xZn_{1-x}Fe_2O_4$ Spinel (*Fd-3m*) PDF # 01-077-9652 24(1)%	$BaTiNiFe_{10}O_{19}$ (*P6$_3$/mmc*) PDF # 00-054-0776 >1% $Ni_{0.8}Zn_{0.2}O$ PDF # 01-071-6735 36(1)%
$BaTiO_3/NiFe_2O_4$ 1300 °C	$BaTiO_3$ Tetragonal (*P4/mmm*) PDF # 01-079-2264 71.1(4)%	$Ni_{0.4}Fe_{2.6}O_4$ Spinel (*Fd-3m*) PDF # 01-087-2335 23.5(3)%	$BaFe_{0.67}Ti_{0.33}O_{2.952}$ PDF # 01-089-0949 (*P6$_3$/mmc*) 5.4(5)%
$BaTiO_3/ZnFe_2O_4$ 1300 °C	$BaTiO_3$ Tetragonal (*P4/mmm*) PDF # 01-079-2264 63.5(3)%	$ZnFe_2O_4$ Spinel (*Fd-3m*) PDF # 01-078-5429 29.6(2)%	$BaFe_{0.125}Ti_{0.875}O_{2.92}$ (*P6$_3$/mmc*) PDF # 01-089-4605 6.9(3)%.
$BaTiO_3/Ni_{0.5}Zn_{0.5}Fe_2O_4$ 1300 °C	$BaTiO_3$ Tetragonal (*P4/mmm*) PDF # 01-079-2264 56(3)%	$Ni_{0.8}Zn_{0.2}Fe_2O_4$ Spinel (*Fd-3m*) PDF # 01-077-9719 34(3)%	$BaFe_{0.25}Ti_{0.75}O_{2.888}$ (*P6$_3$/mmc*) PDF # 01-089-4604 9(1)% $Ni_{0.02}Zn_{0.98}O$ PDF # 01-080-3507 1.0(1)%

The SEM micrographs for as-prepared powders confirmed the presence of two types of particles, different in size and shape, Figure 2. The particles which belong to the $BaTiO_3$ are bigger (0.5–1 μm) in comparison to ferrite particles that are in the sub-100 nm range. It was observed that ferrite particles formed agglomerates due to the size-driven surface activity [66,67]. The EDS maps of these samples confirmed the non-uniform distribution of barium-titanate and ferrite phases. The EDS layered images suggested that the best ferrite distribution over the titanate surface was achieved in the case of the as-prepared $BaTiO_3/NiFe_2O_4$ composite, Figure 2. For the $BaTiO_3/ZnFe_2O_4$ and $BaTiO_3/Ni_{0.5}Zn_{0.5}Fe_2O_4$ powders clear separation of the Zn-rich phases was observed, Figure 2. These results are following XRPD analyses which showed the presence of a zinc oxide phase in the case of $BaTiO_3/ZnFe_2O_4$ (Table 1). Furthermore, the lowest amount of the ferrite phase in the case of $BaTiO_3/ZnFe_2O_4$, observed by XRPD (<30%, Table 2), indicates the sparse distribution of $ZnFe_2O_4$ over the $BaTiO_3$ surface.

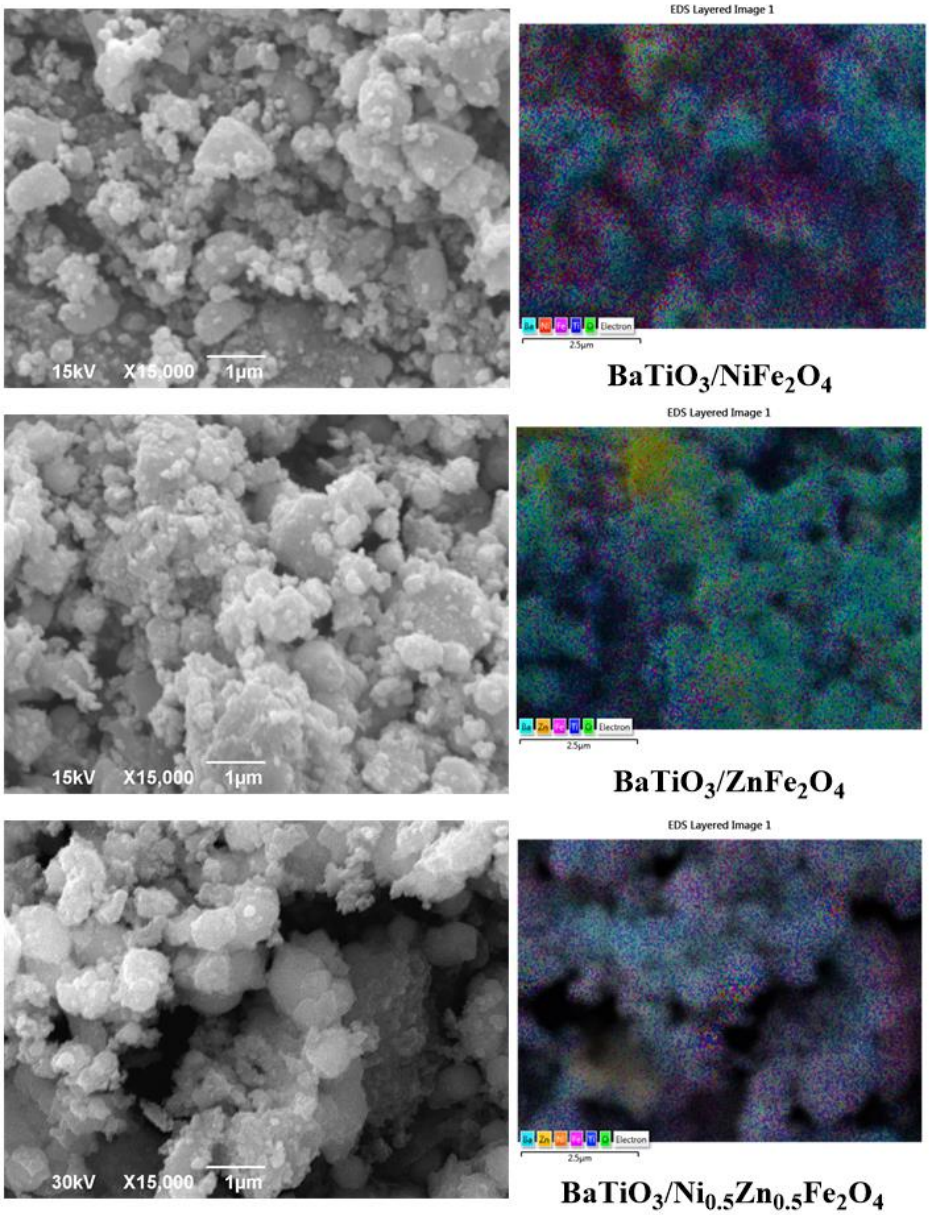

Figure 2. SEM and EDS layered images of non-sintered $BaTiO_3/NiFe_2O_4$, $BaTiO_3/ZnFe_2O_4$, and $BaTiO_3/Ni_{0.5}Zn_{0.5}Fe_2O_4$ samples (Ba-cyan; Zn-yellow; Ni-orange; Fe-magenta; Ti-blue; O-green).

Table 2. Mass magnetization values of sintered samples at room temperature.

Sample	*M* [emu/g]
$BaTiO_3/NiFe_2O_4$ 1150 °C	12.46
$BaTiO_3/ZnFe_2O_4$ 1150 °C	1.74
$BaTiO_3/Ni_{0.5}Zn_{0.5}Fe_2O_4$ 1150 °C	17.26
$BaTiO_3/NiFe_2O_4$ 1300 °C	9.26
$BaTiO_3/ZnFe_2O_4$ 1300 °C	0.06
$BaTiO_3/Ni_{0.5}Zn_{0.5}Fe_2O_4$ 1300 °C	17.91

The SEM micrographs obtained for the samples sintered at 1150 °C revealed that this temperature was not enough to reach the final sintering stage, Figure 3. Most of the particles preserved their initial shape, followed by porosity that is typical for the intermediate sintering stages. EDS mapping of these samples showed the presence of the $BaTiO_3$ cores covered with much smaller ferrite particles forming imperfect shells. However, localized

ferrite phases, especially in the cases of $BaTiO_3/ZnFe_2O_4$ and $BaTiO_3/Ni_{0.5}Zn_{0.5}Fe_2O_4$ were noticed. Moreover and regarding $BaTiO_3/Ni_{0.5}Zn_{0.5}Fe_2O_4$, besides ferrite and barioferrite phases, the occurrence of mixed nickel zinc oxide has been observed, corroborating phase analysis results.

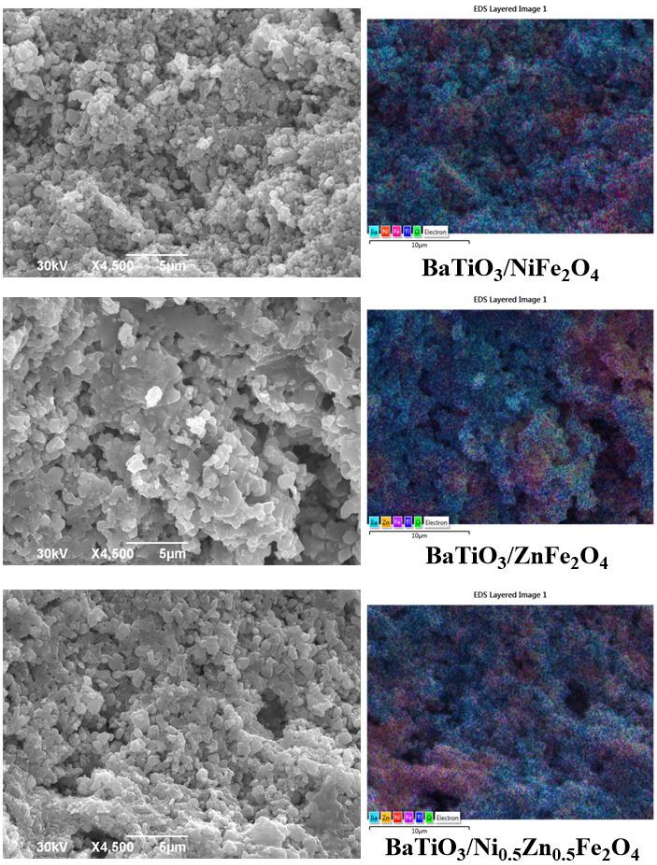

Figure 3. SEM and EDS layered images of $BaTiO_3/NiFe_2O_4$, $BaTiO_3/ZnFe_2O_4$, and $BaTiO_3/Ni_{0.5}Zn_{0.5}Fe_2O_4$ samples sintered at 1150 °C (Ba-cyan; Zn-yellow; Ni-orange; Fe-magenta; Ti-blue; O-green).

The increase in temperature up to 1300 °C led to the occurrence of high-density regions, although some level of porosity was still present, Figure 4. EDS mapping confirmed that ferrite phases were uniformly covered the surface of $BaTiO_3$. For the $BaTiO_3/ZnFe_2O_4$ and $BaTiO_3/Ni_{0.5}Zn_{0.5}Fe_2O_4$ samples, besides core/shell structures the formation of localized Zn-rich phases has been observed.

It should be noticed that the formation of core/shell structures for all sintered samples should have an increased influence on dielectric and ferroelectric properties due to strain effects between ferroelectric $BaTiO_3$ and magnetic ferrite phases. This is in accordance with our previous research on the formation of $BaTiO_3$–Fe_2O_3 core/shell structures, in which we showed that strain originating from the $BaTiO_3$ core strongly affects the electrical properties of the Fe_3O_4 shell, and vice versa [68].

Mass magnetization values at room temperature for the sintered samples are listed in Table 2. Microstructure (grain size) and phase composition, as well as their interplay guide the magnetization process and influence magnetic properties in general [69]. With an increase in sintering temperature up to 1300 °C, different phase composition was obtained (Table 1) and the microstructure was significantly changed (Figures 3 and 4). In the case of $BaTiO_3/NiFe_2O_4$ and $BaTiO_3/ZnFe_2O_4$, the increase in sintering temperature led to the reduction in mass magnetization ($\Delta M/M_0$ = 28.7% and $\Delta M/M_0$ = 97.8% respectively),

while the net magnetization was slightly enhanced for the composite containing mixed Ni,Zn-ferrite ($\Delta M/M_0$ = 13.2%).

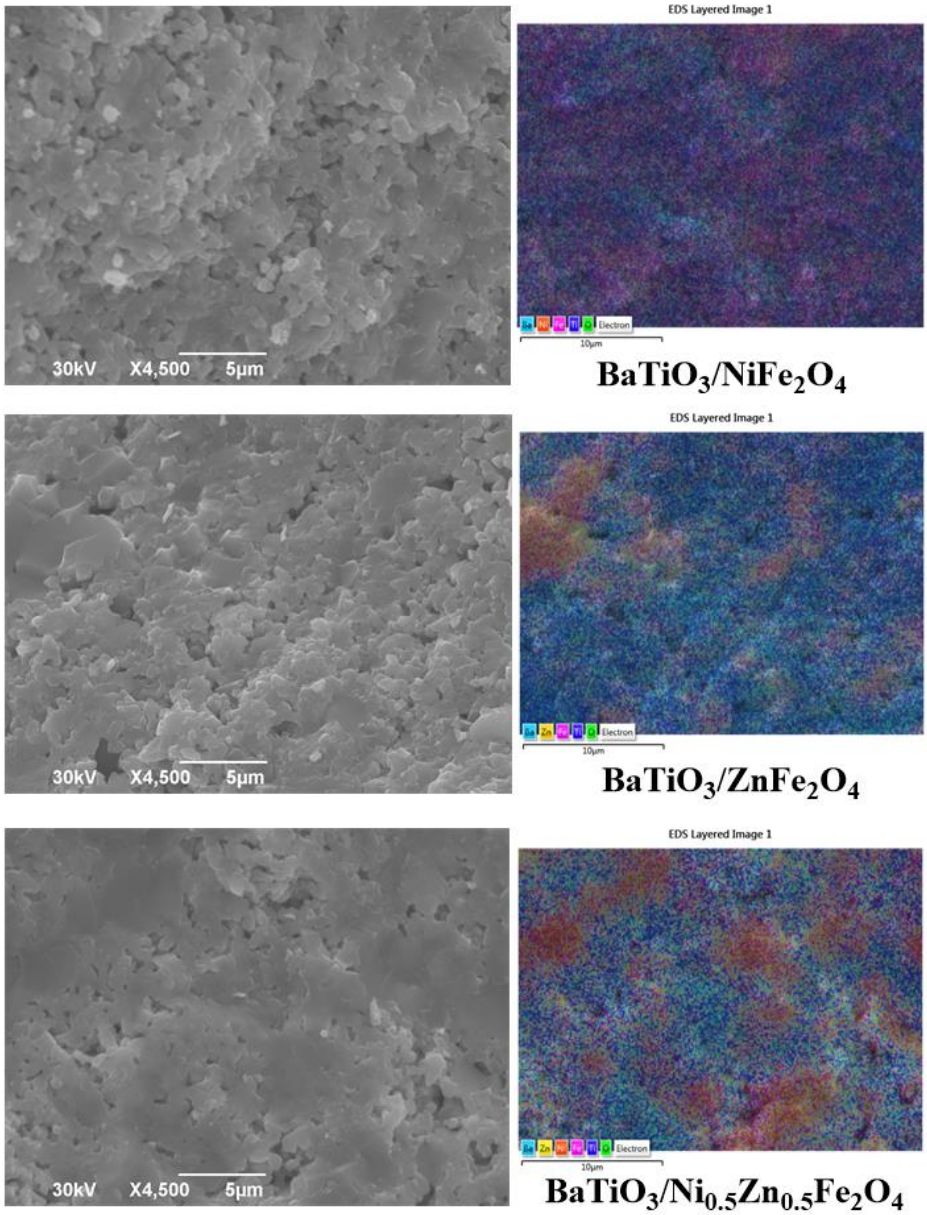

Figure 4. SEM and EDS layered images of $BaTiO_3/NiFe_2O_4$, $BaTiO_3/ZnFe_2O_4$, and $BaTiO_3/Ni_{0.5}Zn_{0.5}Fe_2O_4$ samples sintered at 1300 °C (Ba-cyan; Zn-yellow; Ni-orange; Fe-magenta; Ti-blue; O-green).

In the latter case and in comparison, to $BaTiO_3/NiFe_2O_4$ and $BaTiO_3/ZnFe_2O_4$, mass magnetization enhancement can be explained by the most significant grain size increment as the sintering temperature increased, Figure 4 and Table 2. The change in mass magnetization value in the temperature range from 20 °C to 600 °C under the magnetic field of 50 kA/m for the sintered samples is presented in Figure 5. Magnetization of $BaTiO_3/NiFe_2O_4$ and $BaTiO_3/ZnFe_2O_4$ showed a similar trend upon heating, decreasing slightly, irrespective of sintering temperature. In the case of $BaTiO_3/Ni_{0.5}Zn_{0.5}Fe_2O_4$ sintered at 1150 °C, there was a sharp fall in mass magnetization due to the phase transition caused by partial destruction of the domain structure within the crystallites from 340 °C to 400 °C, followed by a gentle fall in mass magnetization up to 480 °C. Then, the biggest fall due to thermal effects near Curie temperature (T_C) about 540 °C occurred. It was shown

that the $BaTiO_3/NiFe_2O_4$ sintered at 1300 °C has a T_C over 600 °C, while the T_C value of its analogue sintered at 1150 °C is about 600 °C. In the case of $BaTiO_3/Ni_{0.5}Zn_{0.5}Fe_2O_4$ sintered at 1300 °C, T_C is significantly lower (≈420 °C). This can be explained by the fact that Curie temperature decreases with an increase in Zn content due to the weakening of A-B superexchange interaction caused by the replacement of Fe^{3+} by Zn^{2+} ions at tetrahedral sites.

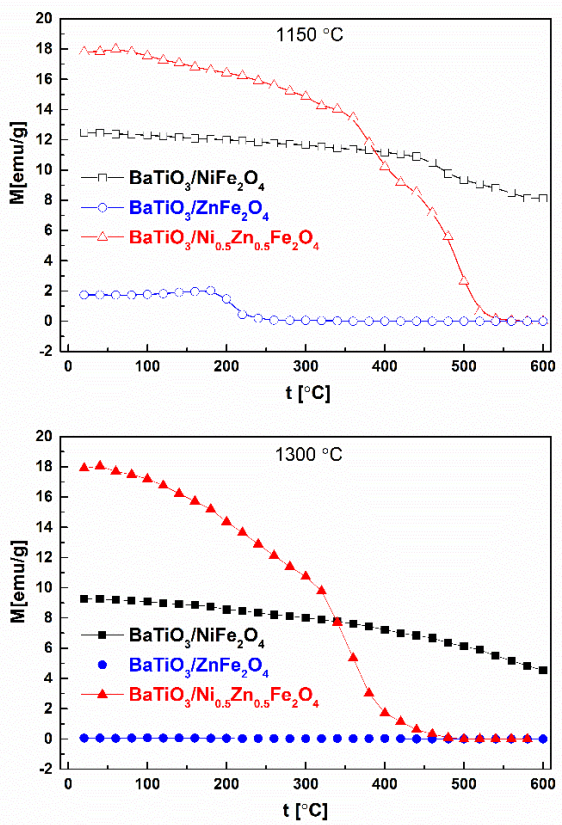

Figure 5. Temperature dependence of mass magnetization in the applied magnetic field of 50 kA/m for all sintered samples.

The relative dielectric constant and the loss tangent as a function of frequency along with corresponding AC conductivity are shown in Figure 6. In the low and mid frequency range, the dielectric constant value decreased with a relatively small slope for all investigated pellets at both sintering temperatures. The reduction in dielectric constant with increasing frequency can be related to Maxwell–Wagner interfacial polarization along with Koop's phenomenological theory [70,71]. The highest value of dielectric constant was observed for $BaTiO_3/Ni_{0.5}Zn_{0.5}Fe_2O_4$ sintered at 1150 °C in the low and mid frequency regions, Figure 6a. In particular cases ε′ and tgδ were greatly increased as a consequence of the highest amount of conductive phases since the influence of the spinel phase on dielectric properties is very strong [72]. Further calcination of this sample led to a lower value of the dielectric constant in the same frequency range. The same was observed in the case of $BaTiO_3/ZnFe_2O_4$, Figure 6a. The dispersion phenomenon in these cases may also originate from the compositional inhomogeneity of formed core/shell structures. The appearance of dielectric relaxation peak at 900 Hz (Figure 6b), recorded for $BaTiO_3/Ni_{0.5}Zn_{0.5}Fe_2O_4$ sintered at 1150 °C might originate from enhanced Maxwell–Wagner polarization between the $BaTiO_3$ phase with higher resistivity and the conductive oxide phases with much lower resistivity. This is in accordance with the research of Yu et al. where the high value of the dielectric constant with frequency relaxation of the $BaTiO_3$-$(Ni_{0.3}Zn_{0.7})Fe_{2.1}O_4$ has been attributed to this type of polarization mechanism [72]. In the case of $BaTiO_3/ZnFe_2O_4$ calcined at the same temperature dielectric relaxation occurred at 90 Hz, Figure 6b. The

obtained results are in agreement with phase composition analysis (Table 1) since the dielectric properties of such composites are mainly determined by the amount of conductive oxide phases. The loss tangents for the samples sintered at 1300 °C are lower in comparison to the loss tangents values of samples sintered at 1150 °C in the low and mid frequency range, Figure 6b. This clearly indicates that the temperature of 1300 °C was high enough to achieve a sufficient sintering yielding dense ceramics. The loss tangents graphs revealed the relaxation in the form of maxima at 0.900 MHz, 1.939 MHz, and 2.8461 MHz for $BaTiO_3/NiFe_2O_4$, $BaTiO_3/Ni_{0.5}Zn_{0.5}Fe_2O_4$, and $BaTiO_3/ZnFe_2O_4$ sintered at 1300 °C, respectively, Figure 6b. The increase in sintering temperature up to 1300 °C led to the slightly higher value of dielectric constant for $BaTiO_3/NiFe_2O_4$ in the frequency range between 1 kHz and 1 MHz, Figure 6a. In the high-frequency region abrupt change of dielectric constant was observed for all samples sintered at 1300 °C, indicating strong frequency dependence, Figure 6a. Generally, the dielectric behaviour of samples sintered at 1300 °C is nearly the same in comparison to their analogues sintered at 1150 °C as a consequence of decreased inhomogeneity in formed core/shell structures. The obvious frequency dispersion in ε′ detected for all sintered pellets was caused by the inhomogeneous structure of the spinel phases. A more pronounced effect was evident for $BaTiO_3/Ni_{0.5}Zn_{0.5}Fe_2O_4$ and $BaTiO_3/ZnFe_2O_4$, corroborating EDS maps where a higher level of localized ferrite shells occurred, Figures 3 and 4.

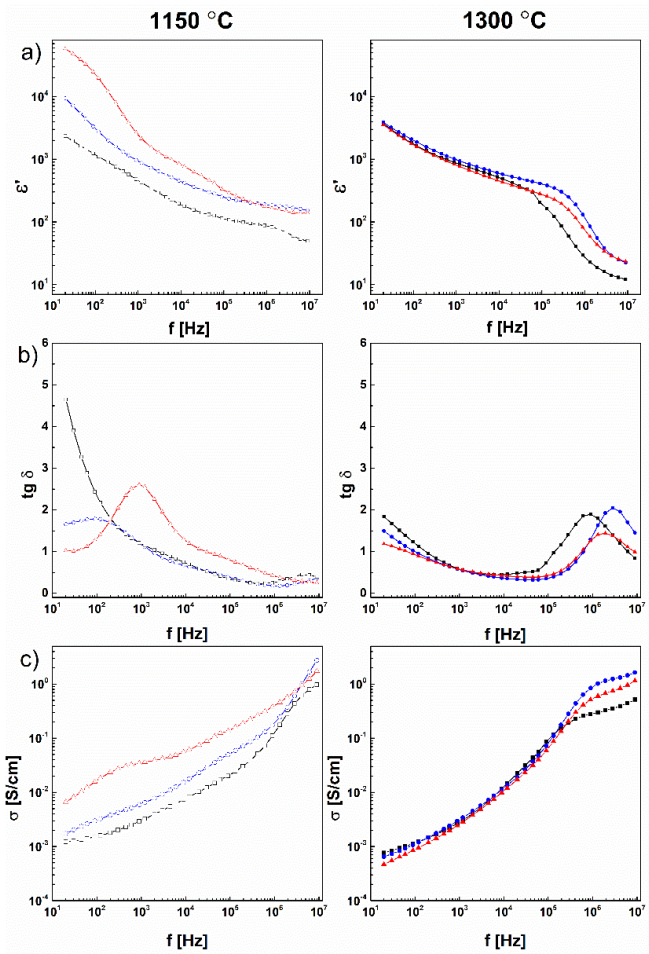

Figure 6. (**a**) Relative dielectric constant and (**b**) tangent loss as a function of frequency with (**c**) AC conductivity for sintered materials. ($BaTiO_3/NiFe_2O_4$—black, $BaTiO_3/ZnFe_2O_4$—blue, and $BaTiO_3/Ni_{0.5}Zn_{0.5}Fe_2O_4$—red.

Figure 6c shows variations in AC conductivity as a function of frequency for the investigated samples. It was noticed that the increase of conductive ferrite phases influenced the

non-linear deviation, while the AC conductivity non-linearly increased with the increase in the frequency, most probably due to heterogeneous conduction and electronic polarization contribution of the ferrite phases [73,74].

The EIS analyzer software and equivalent circuit consisting of two parallel R-CPE elements connected in series were applied for the investigation of relaxation processes. The representative curve for $BaTiO_3/NiFe_2O_4$ sintered at 1150 °C, shown in Figure 7, indicates that experimental data can be fitted with two circles whose centers are not located on the *Z'* axis. This type of modeled circle is typical for the samples which have no single relaxation time (τ), but several of them whose distribution can be presented with mean relaxation time ($\tau_p = \omega_p^{-1}$). This is characteristic of non-Debye relaxation in which the depression angle (θ) relates to the distribution width of the relaxation time due to the non-uniform grain boundary structure of the samples [75]. In our case, non-Debye relaxation originated not only from the porous structure, but from different phases and core-shell structures' grain boundaries. Therefore, the fitting procedure included the use of two CPE instead of typical RC circuits.

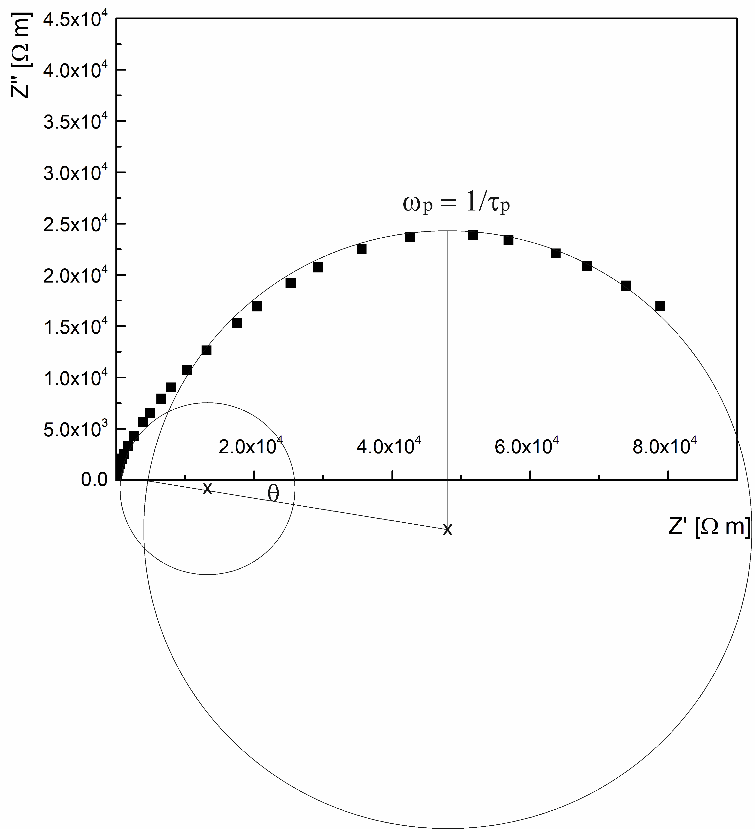

Figure 7. Nuqist plot for $BaTiO_3/NiFe_2O_4$ sintered at 1150 °C.

Variations of relative dielectric constant, tangent loss, and AC conductivity with the frequency for the selected temperature range (150–400 K) for all sintered samples are displayed in Figures 8–10, respectively. The relative dielectric constant value is continuously reduced, exhibiting a plateau in the high-frequency region, irrespective of the investigated sample, Figure 8. The increase in permittivity in the low-frequency region with an increase in temperature can be addressed by nano-inhomogeneous conductivity of ferrite phases [76,77]. The frequency-dependent tangent loss values for the samples sintered at 1150 °C show a typical behavior of composites with inhomogeneous conductivity. Interestingly, in the case of samples sintered at 1300 °C, in the high-temperature range, the values of high-frequency tangent loss increased due to the defects in the material, including oxygen vacancies and transformation of $BaTiO_3$ from *P4mm* to *P4/mmm* space group, Figure 9. From the AC

conductivity spectra, presented in Figure 10, it is obvious that the conductivity exhibited a twist of about 10^4 Hz, deviating from the classical Jonsher relationship [78].

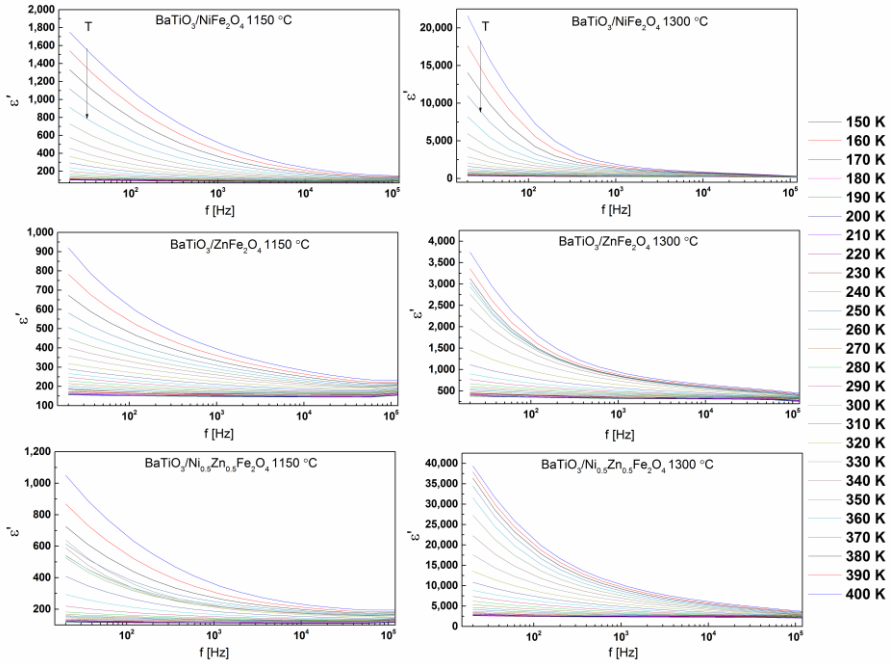

Figure 8. Relative dielectric constant spectra of the sintered samples and their temperature dependence.

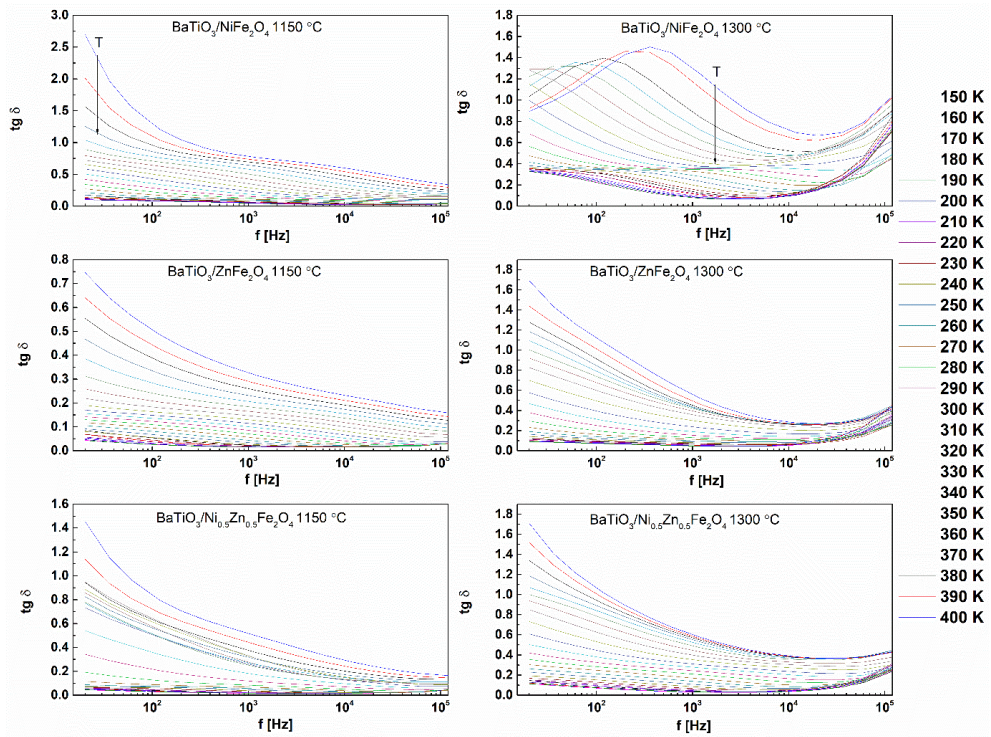

Figure 9. Tangent loss as a function of the frequency of the sintered samples and its temperature dependence.

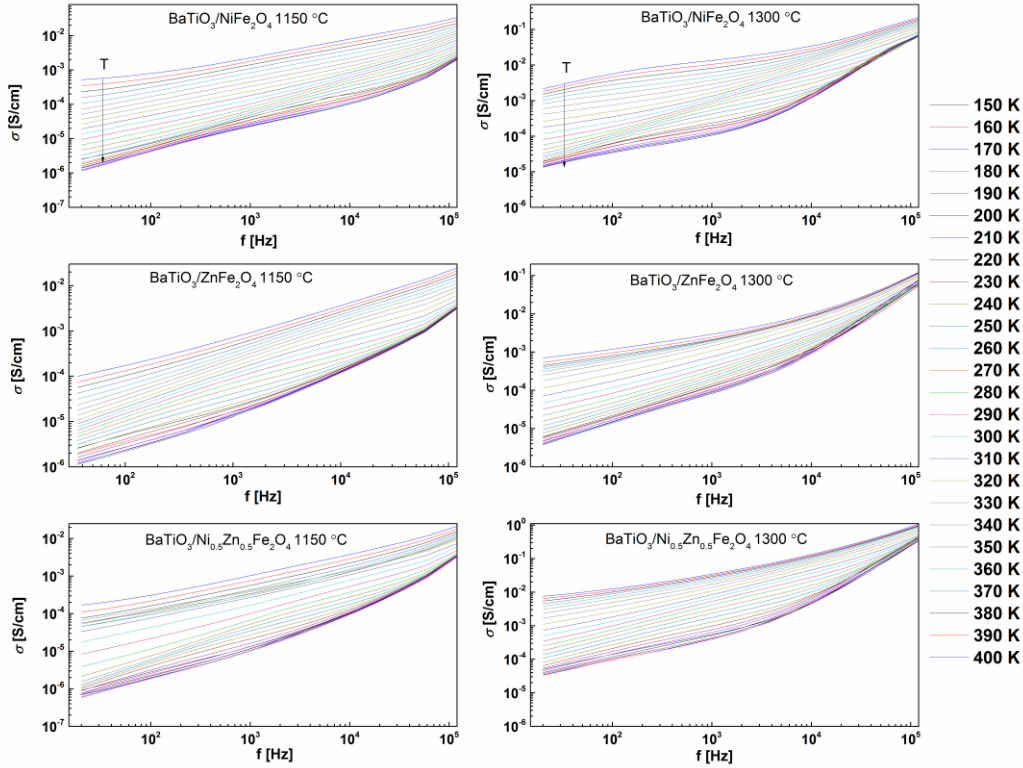

Figure 10. Conductivity spectra of the sintered samples and their temperature dependence.

The non-linear dependence in P-E measurements indicated typical behavior for ferroelectric composites where the structure inhomogeneity can lead to uncharacteristic forms of hysteresis loops. This type of inhomogeneity mainly originates from the presence of a large amount of spinel ferrite phase in the core/shell structures and localized regions of agglomerated ferrites.

The P-E loops for all sintered samples at a fixed frequency of 100 Hz and electrical field of 10 kV/cm are given in the Supplementary material (Figure S1), while a typical hysteresis curve for sample $BaTiO_3/NiFe_2O_4$ sintered at 1150 °C at the fields of 20 kV/cm is presented in Figure 11. In this sample, the amount of ferroelectric $BaTiO_3$ tetragonal (*P4mm*) phase was 77(2)%, i.e., the highest among all investigated sintered samples, while the amount of conductive ferrite/barioferrite phases was the lowest, Table 1. The increase of the barium-titanate phase led to the decrease of the coercive field. For the $BaTiO_3/ZnFe_2O_4$ and $BaTiO_3/Ni_{0.5}Zn_{0.5}Fe_2O_4$ samples sintered at 1150 °C, where the localization of Zn-rich phases has been observed by EDS mappings, hysteresis loops shape was strongly affected by the large amount of conductive phases in the composites (see Figure S1 and Figure 3, and Table 1). The increase in temperature up to 1300 °C led to the transformation of $BaTiO_3$ from *P4mm* to *P4/mmm* space group in all three cases, Table 1. The highest amount of non-centrosymmetric phase was observed for $BaTiO_3/NiFe_2O_4$ sintered at 1300 °C, significantly deteriorating the ferroelectric hysteresis loop, Figure S1. The ferroelectric hysteresis loop shape was mostly influenced in the case of $BaTiO_3/Ni_{0.5}Zn_{0.5}Fe_2O_4$ sintered at 1300 °C in comparison to its analogue sintered at 1150 °C, since the conductive phases amount was reduced (see Table 1).

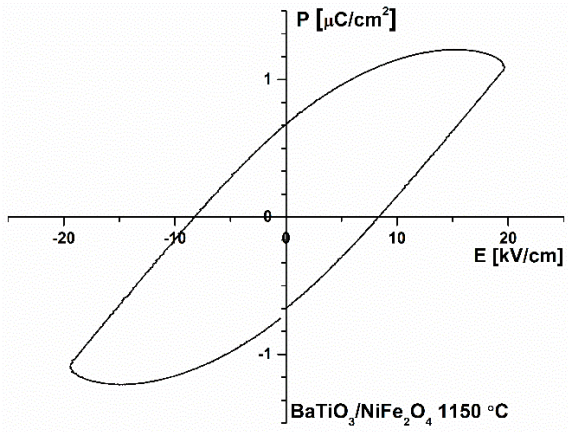

Figure 11. Hysteresis loop of $BaTiO_3/NiFe_2O_4$ sintered at 1150 °C at 20 kV/cm field.

The presence of spinel phases alongside with Maxwell-Wagner interfacial polarization influenced the hysteresis loops shapes. Furthermore, the deviation from the ferroelectric behavior of investigated composites might originate from the formation of core-shell structures where ferrite agglomerates surrounded $BaTiO_3$ particles. Therefore, it is very hard to determine the values of saturation polarization and coercive field from the presented ferroelectric loops [79].

The leakage current density (j) as a function of static electric field (E) on semi-logarithmic plots were presented in Figure 12. The highest value of leakage current was obtained for $BaTiO_3/Ni_{0.5}Zn_{0.5}Fe_2O_4$ sintered at 1150 °C, due to the highest amount of the conductive nickel, and zinc oxide phases, Figure 12a and Table 1. This is in accordance with the dielectric spectra presented in Figure 6b, where the dielectric loss was significant (at 900 Hz). On the other hand, the lowest value of leakage current density was found in the sample with the highest concentration of barium titanate phase ($BaTiO_3/NiFe_2O_4$ sintered at 1150 °C). The increase in sintering temperature reduced the amount of the conductive nickel zinc oxide phases in $BaTiO_3/Ni_{0.5}Zn_{0.5}Fe_2O_4$ (see Table 1), leading to a slight decrease of the current leakage, Figure 12.

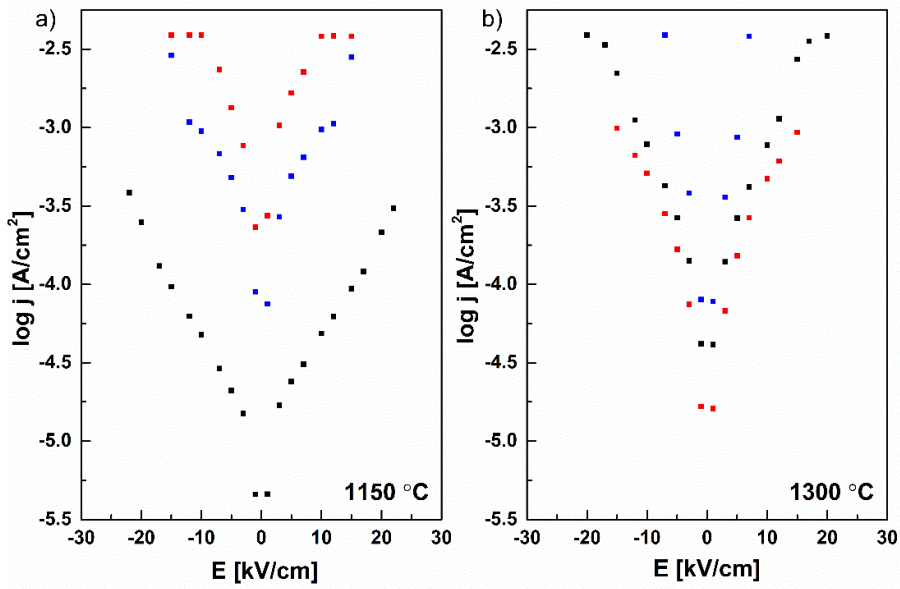

Figure 12. Leakage current measurements for the samples (**a**) sintered at 1150 °C, (**b**) sintered at 1300 °C ($BaTiO_3/NiFe_2O_4$—black, $BaTiO_3/ZnFe_2O_4$—blue, and $BaTiO_3/Ni_{0.5}Zn_{0.5}Fe_2O_4$—red) as log j—E dependence.

To illustrate the conduction mechanism in the investigated ceramics, plots log j versus log E were recorded, Figure 13. It should be emphasized that the range of the applied electric field was not the same for all investigated samples due to different compositions and microstructure inhomogeneity. Furthermore, in this type of experiment, the effective distance between the electrodes during the measurements may vary, which could cause dielectric breakdown and additionally complicate the interpretation of the experimental data. Taking all this into account, although many studies explain the conduction in such materials by four possible mechanisms (grain boundary limited conduction (GBLC), ohmic conduction mechanism, space charge limited conduction (SCLC), or trap-controlled SCLC mechanism) [80,81], the measured room-temperature leakage current density and its dependence on the static electric field in such complex composites cannot be easily interpreted. However, the presence of the ohmic conduction mechanism was undoubted for all investigated samples, Figure 13.

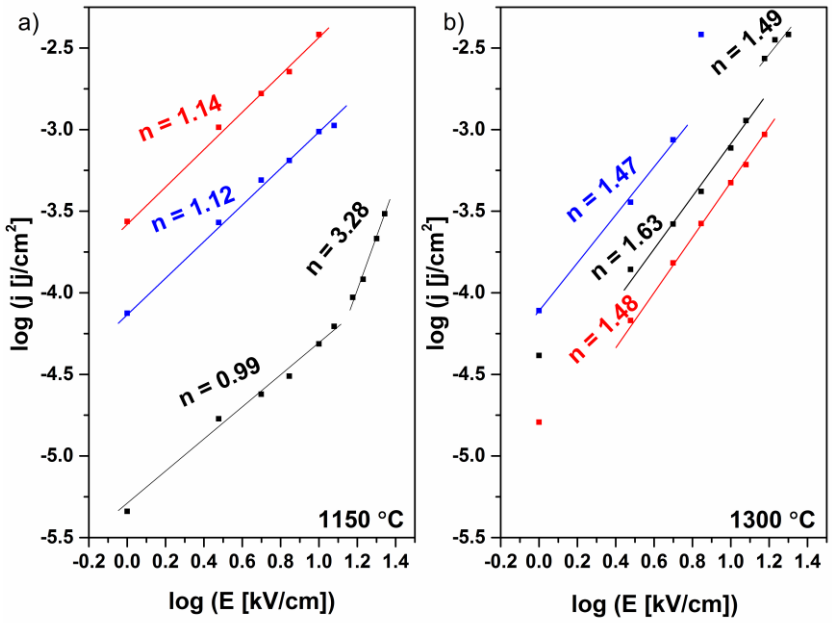

Figure 13. Leakage current measurements for the samples (**a**) sintered at 1150 °C, (**b**) sintered at 1300 °C ($BaTiO_3/NiFe_2O_4$—black, $BaTiO_3/ZnFe_2O_4$—blue, and $BaTiO_3/Ni_{0.5}Zn_{0.5}Fe_2O_4$—red) as log j—log E dependence; n represents the slope of the curves in logarithmic plots.

3. Materials and Methods

3.1. Synthesis

All chemicals (barium titanate ($BaTiO_3$, 99%), acetylacetone, ammonium hydroxide solution (28% NH_3 in water), iron(III) chloride hexahydrate ($FeCl_3 \cdot 6H_2O$, 98%), nickel(II) chloride hexahydrate ($NiCl_2 \cdot 6H_2O$, 98%), zinc(II) chloride ($ZnCl_2$, 98%), toluene (99.8%)) were obtained from Sigma-Aldrich.

All investigated ferrites ($NiFe_2O_4$, $ZnFe_2O_4$, $Ni_{0.5}Zn_{0.5}Fe_2O_4$) were in situ prepared on $BaTiO_3$ particles by thermal decomposition method from appropriate acetylacetonate complexes ([$Fe(acac)_3$], [$Ni(acac)_2$], and [$Zn(acac)_2$], where acac presents acetylacetonate anion). The iron(III) acetylacetonate, nickel(II) acetylacetonate, and zinc(II) acetylacetonate were synthesized in a reaction of appropriate metal ions (Fe^{3+}, Ni^{2+}, Zn^{2+}) with ammonium acetylacetonate. The synthesis procedure for obtaining such ferrite systems was previously described by Andjelkovic et al. [82]. Briefly, a stoichiometric amount of $BaTiO_3$ and appropriate acetylacetonate complexes necessary to obtain 0.013 mol of ferrite/titanate composite were used. The thermal decomposition of the mixture suspended in toluene was performed in an electrical furnace with a heating rate of 10 °C/min at t = 500 °C for 1 h, followed by pulverization in an agate mortar.

After the initial preparation protocols, the as-prepared powders were compressed into the pellets at 300 MPa using a uniaxial double action pressing process with an 8 mm diameter tool, hydraulic press RING, P-14, and VEB THURINGER. The pellets were sintered at the temperatures of 1150 °C and 1300 °C in an electrical tube furnace equipped with a LAND calibration source, with a heating rate of 15 °C/min to 1000 °C and 5 °C/min until chosen temperatures were reached for 2.5 h. The sintered samples were removed from the electrical tube furnace after spontaneously cooling to room temperature.

3.2. Characterization

X-ray powder diffraction (XRPD) patterns were collected using Ultima IV Rigaku diffractometer with $CuK_{\alpha 1,2}$ radiation (U = 40.0 kV, I = 40.0 mA) equipped with D/TeX Ultra high—speed detector. The diffraction angle range was 10–80° 2θ with a step of 0.02°. at a scan speed of 5°/min. The phase composition of the synthesized materials, as well as, phase abundances are calculated by the RIR method incorporated in PDXL2 integrated X-ray powder diffraction software (Version 2.8.30; Rigaku Corporation, Tokyo, Japan).

The morphology and composition of the prepared composites were determined by scanning electron microscopy (SEM) performed on JEOL JSM-6390 LV coupled with electron dispersive spectroscopy (Oxford Instruments X-MaxN). The accelerating voltage was in the range of 20 and 30 kV.

Mass magnetization measurements were performed according to a modified Faraday method using a laboratory weighing scale (Sartorius PRACTUM 124-1S) with a sensitivity of 10^{-7} kg and a magnetic field strength at the sample placement site of 50 kA/m. The heating rate was 20 °C/min.

Dielectric properties of the sintered samples were determined by two digital LCR meters: Hameg 8118 (from 20 Hz to 90 kHz) and Agilent 4285A (from 90 kHz to 9 MHz), under normal atmospheric pressure, ambient temperature, and relative humidity of 40%. The applied voltage across the closed micrometer capacitor cell was 1.5 V. The capacitor cell was housed in a Faraday cage. To obtain broader frequency dependence of dielectric parameters (tg δ, ε′, Z′, Z″), frequency spectra were merged.

To perform temperature dependence measurements pellets were placed in a vacuum chamber with a cold head and capacitor cell mounted on it. Pfeiffer vacuum turbo molecular pump maintained 10^{-4} mbar pressure. CTI Cryogenics refrigerating system model 22 mounted on the cold head was applied to a lower temperature to 150 K. Lakeshore 340 temperature controller with hater attached at the cold head was used to gradual heating rate of 2.5 K/min up to 400 K.

Ferroelectric and leakage current measurements were conducted in the electrical field range of 5–40 kV/cm on the Precision Multiferroic Test System with High Voltage Interface (Radiant Technologies, Inc., Albuquerque, New Mexico).

4. Conclusions

The aim of this study was the investigation of the effect of phase composition on the magnetic, dielectric, and ferroelectric properties of $BaTiO_3/Ni_xZn_{1-x}Fe_2O_4$ (x = 0, 0.5, 1) ceramic composites. Powders, $NiFe_2O_4$, $ZnFe_2O_4$, and $Ni_{0.5}Zn_{0.5}Fe_2O_4$, were in situ synthesized by thermal decomposition of acetylacetonate precursors onto $BaTiO_3$ surface and additionally sintered at two chosen temperatures (1150 °C and 1300 °C) to obtain dense ceramics. Since phase composition and morphology have a significant influence on the material functional properties, the XRPD, as well as SEM was performed and the results were evaluated in detail. Generally, the spinel and perovskite phases were dominant for as-prepared materials, while spinel, perovskite, and barioferrite-like phases in different ratios prevailed in the case of sintered samples. Although the final sintering stage was not reached at both chosen temperatures, a significantly better sintering effect was noticed at 1300 °C, especially in the composite containing mixed Ni,Zn-ferrite where the mass magnetization was slightly enhanced with an increase in sintering temperature. It was concluded that the dielectric and ferroelectric properties of investigated composites are

mainly determined by the amount of conductive oxide phases, the formation of core-shell structures, and microstructure inhomogeneity.

Supplementary Materials: The following supporting information can be downloaded at: https://www.mdpi.com/article/10.3390/inorganics11020051/s1, Figure S1: Electrical hysteresis loops for sintered samples.

Author Contributions: Conceptualization, L.A.; Methodology, M.Š. and L.A.; Investigation, M.Š., I.P., M.M.M., A.D., A.K., V.B.P., A.K.-G. and L.A.; Resources, M.Š., I.P., M.M.M., A.D., A.K., V.B.P., A.K.-G. and L.A.; Writing—Original Draft, M.Š. and L.A.; Writing—review and editing, M.Š., V.B.P. and L.A.; Supervision, L.A. All authors have read and agreed to the published version of the manuscript.

Funding: The authors would like to thank the Ministry of Education, Science and Technological Development of Republic of Serbia (Grant Nos. 451-03-68/2022-14/200026, 451-03-68/2022-14/200126, 451-03-68/2022-14/200162, 451-03-68/2022-14/200053, 451-03-68/2022-14/200017, 451-03-68/2022-14/200132 and 451-03-68/2022-14/200116) for financial support.

Data Availability Statement: No new data were created or analyzed in this study. Data sharing is not applicable to this article.

Conflicts of Interest: The authors declare no conflict of interest.

References

1. Jana, B.; Ghosh, K.; Rudrapal, K.; Gaur, P.; Shihabudeen, P.K.; Roy Chaudhuri, A. Recent Progress in Flexible Multiferroics. *Front. Phys.* **2022**, *9*, 810. [CrossRef]
2. Fiebig, M.; Lottermoser, T.; Meier, D.; Trassin, M. The evolution of multiferroics. *Nat. Rev. Mater.* **2016**, *1*, 16046. [CrossRef]
3. Kimura, T.; Kawamoto, S.; Yamada, I.; Azuma, M.; Takano, M.; Tokura, Y. Magnetocapacitance effect in multiferroic $BiMnO_3$. *Phys. Rev. B* **2003**, *67*, 180401. [CrossRef]
4. Wang, J.; Neaton, J.B.; Zheng, H.; Nagarajan, V.; Ogale, S.B.; Liu, B.; Viehland, D.; Vaithyanathan, V.; Schlom, D.G.; Waghmare, U.V.; et al. Epitaxial $BiFeO_3$ Multiferroic Thin Film Heterostructures. *Science* **2003**, *299*, 1719–1722. [CrossRef] [PubMed]
5. Srinivasan, G. Magnetoelectric composites. *Annu. Rev. Mater. Res.* **2010**, *40*, 153–178. [CrossRef]
6. Ma, J.; Hu, J.; Li, Z.; Nan, C.-W. Recent Progress in Multiferroic Magnetoelectric Composites: From Bulk to Thin Films. *Adv. Mater.* **2011**, *23*, 1062–1087. [CrossRef] [PubMed]
7. Pradhan, D.K.; Kumari, S.; Rack, P.D. Magnetoelectric Composites: Applications, Coupling Mechanisms, and Future Directions. *Nanomaterials* **2020**, *10*, 2072. [CrossRef]
8. Mao, Q.; Wu, J.; Hu, Z.; Xu, Y.; Du, Y.; Hao, Y.; Guan, M.; Wang, C.; Wang, Z.; Zhou, Z.; et al. Magnetoelectric devices based on magnetoelectric bulk composites. *J. Mater. Chem. C* **2021**, *9*, 5594–5614. [CrossRef]
9. Hu, J.-M.; Duan, C.-G.; Nan, C.-W.; Chen, L.-Q. Understanding and designing magnetoelectric heterostructures guided by computation: Progresses, remaining questions, and perspectives. *Npj Comput. Mater.* **2017**, *3*, 18. [CrossRef]
10. Liu, H.; Yang, X. A brief review on perovskite multiferroics. *Ferroelectrics* **2017**, *507*, 69–85. [CrossRef]
11. Dong, S.; Liu, J.-M. Recent Progress of Multiferroic Perovskite Manganites. *Mod. Phys. Lett. B* **2012**, *26*, 1230004. [CrossRef]
12. Saini, J.; Sharma, A.; Sharma, M.; Kuanr, B.K. Yttrium iron garnet (YIG)/barium titanate (BTO) an engineered multiferroic nanocomposite. *J. Alloys Compd.* **2021**, *879*, 160422. [CrossRef]
13. Wang, X.; Chai, Y.; Zhou, L.; Cao, H.; Cruz, C.; Yang, J.; Dai, J.; Yin, Y.; Yuan, Z.; Zhang, S.; et al. Observation of Magnetoelectric Multiferroicity in a Cubic Perovskite System: $LaMn_3Cr_4O_{12}$. *Phys. Rev. Lett.* **2015**, *115*, 87601. [CrossRef] [PubMed]
14. Takahashi, Y.; Shimano, R.; Kaneko, Y.; Murakawa, H.; Tokura, Y. Magnetoelectric resonance with electromagnons in a perovskite helimagnet. *Nat. Phys.* **2012**, *8*, 121–125. [CrossRef]
15. Kopyl, S.; Surmenev, R.; Surmeneva, M.; Fetisov, Y.; Kholkin, A. Magnetoelectric effect: Principles and applications in biology and medicine—A review. *Mater. Today Bio* **2021**, *12*, 100149. [CrossRef]
16. Cai, T.-Y.; Liu, S.-C.; Ju, S.; Liu, C.-Y.; Guo, G.-Y. Multiferroic Double Perovskites $ScFe_{1-x}CrO_3$ ($1/6 \leq x \leq 5/6$) for Highly Efficient Photovoltaics and Spintronics. *Phys. Rev. Appl.* **2017**, *8*, 34034. [CrossRef]
17. Huang, W.; Harnagea, C.; Benetti, D.; Chaker, M.; Rosei, F.; Nechache, R. Multiferroic Bi_2FeCrO_6 based p–i–n heterojunction photovoltaic devices. *J. Mater. Chem. A* **2017**, *5*, 10355–10364. [CrossRef]
18. Nechache, R.; Harnagea, C.; Li, S.; Cardenas, L.; Huang, W.; Chakrabartty, J.; Rosei, F. Bandgap tuning of multiferroic oxide solar cells. *Nat. Photonics* **2015**, *9*, 61–67. [CrossRef]
19. Vavilapalli, D.S.; Srikanti, K.; Mannam, R.; Tiwari, B.; Mohan Kant, K.; Rao, M.S.R.; Singh, S. Photoactive Brownmillerite Multiferroic $KBiFe_2O_5$ and Its Potential Application in Sunlight-Driven Photocatalysis. *ACS Omega* **2018**, *3*, 16643–16650. [CrossRef]
20. Sun, B.; Zhou, G.; Sun, L.; Zhao, H.; Chen, Y.; Yang, F.; Zhao, Y.; Song, Q. ABO_3 multiferroic perovskite materials for memristive memory and neuromorphic computing. *Nanoscale Horiz.* **2021**, *6*, 939–970. [CrossRef]

21. Plyushch, A.; Macutkevič, J.; Sokal, A.; Lapko, K.; Kudlash, A.; Adamchuk, D.; Ksenevich, V.; Bychanok, D.; Selskis, A.; Kuzhir, P.; et al. The Phosphate-Based Composite Materials Filled with Nano-Sized $BaTiO_3$ and Fe_3O_4: Toward the Unfired Multiferroic Materials. *Materials* **2021**, *14*, 133. [CrossRef] [PubMed]
22. Omelyanchik, A.; Antipova, V.; Gritsenko, C.; Kolesnikova, V.; Murzin, D.; Han, Y.; Turutin, A.V.; Kubasov, I.V.; Kislyuk, A.M.; Ilina, T.S.; et al. Boosting Magnetoelectric Effect in Polymer-Based Nanocomposites. *Nanomaterials* **2021**, *11*, 1154. [CrossRef] [PubMed]
23. Homes, C.C.; Dordevic, S.V.; Strongin, M.; Bonn, D.A.; Liang, R.; Hardy, W.H.; Komiya, S.; Ando, Y.; Yu, G.; Kaneko, N.; et al. A universal scaling relation in high-temperature superconductors. *Nature* **2004**, *430*, 539–541. [CrossRef]
24. Martins, P.; Larrea, A.; Gonçalves, R.; Botelho, G.; Ramana, E.V.; Mendiratta, S.K.; Sebastian, V.; Lanceros-Mendez, S. Novel Anisotropic Magnetoelectric Effect on δ-FeO(OH)/P(VDF-TrFE) Multiferroic Composites. *ACS Appl. Mater. Interfaces* **2015**, *7*, 11224–11229. [CrossRef]
25. Corral-Flores, V.; Bueno-Baqués, D.; Ziolo, R.F. Synthesis and characterization of novel $CoFe_2O_4$–$BaTiO_3$ multiferroic core–shell-type nanostructures. *Acta Mater.* **2010**, *58*, 764–769. [CrossRef]
26. Chermahini, M.D.; Shahraki, M.M.; Kazazi, M. Multiferroic properties of novel lead-free KNN-LT/20NZCFO magneto-electric composites. *Mater. Lett.* **2018**, *233*, 188–190. [CrossRef]
27. Wang, Y.; Hu, J.; Lin, Y.; Nan, C.-W. Multiferroic magnetoelectric composite nanostructures. *NPG Asia Mater.* **2010**, *2*, 61–68. [CrossRef]
28. Jayachandran, K.P.; Guedes, J.M.; Rodrigues, H.C. Solutions for maximum coupling in multiferroic magnetoelectric composites by material design. *Sci. Rep.* **2018**, *8*, 4866. [CrossRef]
29. Feng, M.; Wang, J.; Hu, J.-M.; Wang, J.; Ma, J.; Li, H.-B.; Shen, Y.; Lin, Y.-H.; Chen, L.-Q.; Nan, C.-W. Optimizing direct magnetoelectric coupling in Pb(Zr,Ti)O_3/Ni multiferroic film heterostructures. *Appl. Phys. Lett.* **2015**, *106*, 72901. [CrossRef]
30. Gupta, A.; Chatterjee, R. Dielectric and magnetoelectric properties of $BaTiO_3$–$Co_{0.6}Zn_{0.4}Fe_{1.7}Mn_{0.3}O_4$ composite. *J. Eur. Ceram. Soc.* **2013**, *33*, 1017–1022. [CrossRef]
31. Gorige, V.; Kati, R.; Yoon, D.H.; Kumar, P.S.A. Strain mediated magnetoelectric coupling in a $NiFe_2O_4$–$BaTiO_3$ multiferroic composite. *J. Phys. D Appl. Phys.* **2016**, *49*, 405001. [CrossRef]
32. Yang, S.-C.; Kumar, A.; Petkov, V.; Priya, S. Room-temperature magnetoelectric coupling in single-phase $BaTiO_3$-$BiFeO_3$ system. *J. Appl. Phys.* **2013**, *113*, 144101. [CrossRef]
33. Patil, D.; Kim, J.-H.; Chai, Y.S.; Nam, J.-H.; Cho, J.-H.; Kim, B.-I.; Kim, K.H. Large Longitudinal Magnetoelectric Coupling in $NiFe_2O_4$–$BaTiO_3$ Laminates. *Appl. Phys. Express* **2011**, *4*, 73001. [CrossRef]
34. Martínez-Pérez, J.P.; Bolarín-Miró, A.M.; Cortés-Escobedo, C.A.; Sánchez-De Jesús, F. Magnetodielectric coupling in barium titanate–cobalt ferrite composites obtained via thermally-assisted high-energy ball milling. *Ceram. Int.* **2022**, *48*, 9527–9533. [CrossRef]
35. Dzunuzovic, A.S.; Petrovic, M.M.V.; Stojadinovic, B.S.; Ilic, N.I.; Bobic, J.D.; Foschini, C.R.; Zaghete, M.A.; Stojanovic, B.D. Multiferroic (NiZn) Fe_2O_4–$BaTiO_3$ composites prepared from nanopowders by auto-combustion method. *Ceram. Int.* **2015**, *41*, 13189–13200. [CrossRef]
36. Etier, M.; Schmitz-Antoniak, C.; Salamon, S.; Trivedi, H.; Gao, Y.; Nazrabi, A.; Landers, J.; Gautam, D.; Winterer, M.; Schmitz, D.; et al. Magnetoelectric coupling on multiferroic cobalt ferrite–barium titanate ceramic composites with different connectivity schemes. *Acta Mater.* **2015**, *90*, 1–9. [CrossRef]
37. Hossain, S.; Hossain, S. Magnetic and Optical Characterization of Cobalt Ferrite–Barium Titanate Core–Shell for Biomedical Applications. *IEEE Trans. Magn.* **2022**, *58*, 2501208. [CrossRef]
38. Sreenivasulu, G.; Qu, H.; Srinivasan, G. Multiferroic oxide composites: Synthesis, characterisation and applications. *Mater. Sci. Technol.* **2014**, *30*, 1625–1632. [CrossRef]
39. Ryu, J.; Carazo, A.V.; Uchino, K.; Kim, H.-E. Piezoelectric and magnetoelectric properties of lead zirconate titanate/Ni-ferrite particulate composites. *J. Electroceramics* **2001**, *7*, 17–24. [CrossRef]
40. Hrib, L.M.; Caltun, O.F. Effects of the chemical composition of the magnetostrictive phase on the dielectric and magnetoelectric properties of cobalt ferrite–barium titanate composites. *J. Alloys Compd.* **2011**, *509*, 6644–6648. [CrossRef]
41. Grigalaitis, R.; Vijatović Petrović, M.M.; Bobić, J.D.; Dzunuzovic, A.; Sobiestianskas, R.; Brilingas, A.; Stojanović, B.D.; Banys, J. Dielectric and magnetic properties of $BaTiO_3$-$NiFe_2O_4$ multiferroic composites. *Ceram. Int.* **2014**, *40*, 6165–6170. [CrossRef]
42. El-Shater, R.E.; Atlam, A.S.; Elnimr, M.K.; Assar, S.T.; Tishkevich, D.I.; Zubar, T.I.; Trukhanov, S.V.; Trukhanov, A.V.; Zhou, D.; Darwish, M.A. AC measurements, impedance spectroscopy analysis, and magnetic properties of $Ni_{0.5}Zn_{0.5}Fe_2O_4$/$BaTiO_3$ multiferroic composites. *Mater. Sci. Eng. B* **2022**, *286*, 116025. [CrossRef]
43. De Leo, C.T.; Dannangoda, G.C.; Hobosyan, M.A.; Held, J.T.; Samghabadi, F.S.; Khodadadi, M.; Litvinov, D.; Mkhoyan, K.A.; Martirosyan, K.S. Carbon combustion synthesis of Janus-like particles of magnetoelectric cobalt ferrite and barium titanate. *Ceram. Int.* **2021**, *47*, 5415–5422. [CrossRef]
44. Matutes-Aquino, J.A.; Botello-Zubiate, M.E.; Corral-Flores, V.; Frutos, J.D.E.; Cebollada, F.; Menéndez, E.; Jiménez, F.J.; González, A.M. Synthesis and Characterization of Nickel Ferrite-Barium Titanate Ceramic Composites. *Integr. Ferroelectr.* **2008**, *101*, 22–28. [CrossRef]
45. Safi Samghabadi, F.; Chang, L.; Khodadadi, M.; Martirosyan, K.S.; Litvinov, D. Scalable, cost-efficient synthesis and properties optimization of magnetoelectric cobalt ferrite/barium titanate composites. *APL Mater.* **2021**, *9*, 21104. [CrossRef]

46. Majid, F.; Rauf, J.; Ata, S.; Bibi, I.; Malik, A.; Ibrahim, S.M.; Ali, A.; Iqbal, M. Synthesis and characterization of $NiFe_2O_4$ ferrite: Sol–gel and hydrothermal synthesis routes effect on magnetic, structural and dielectric characteristics. *Mater. Chem. Phys.* **2021**, *258*, 123888. [CrossRef]
47. Majid, F.; Rauf, J.; Ata, S.; Bibi, I.; Yameen, M.; Iqbal, M. Hydrothermal Synthesis of Zinc Doped Nickel Ferrites: Evaluation of Structural, Magnetic and Dielectric Properties. *Z. Für Phys. Chemie* **2019**, *233*, 1411–1430. [CrossRef]
48. Rodríguez-Rodríguez, A.A.; Moreno-Trejo, M.B.; Meléndez-Zaragoza, M.J.; Collins-Martínez, V.; López-Ortiz, A.; Martínez-Guerra, E.; Sánchez-Domínguez, M. Spinel-type ferrite nanoparticles: Synthesis by the oil-in-water microemulsion reaction method and photocatalytic water-splitting evaluation. *Int. J. Hydrogen Energy* **2019**, *44*, 12421–12429. [CrossRef]
49. Atiq, S.; Majeed, M.; Ahmad, A.; Abbas, S.K.; Saleem, M.; Riaz, S.; Naseem, S. Synthesis and investigation of structural, morphological, magnetic, dielectric and impedance spectroscopic characteristics of Ni-Zn ferrite nanoparticles. *Ceram. Int.* **2017**, *43*, 2486–2494. [CrossRef]
50. Thakur, P.; Taneja, S.; Chahar, D.; Ravelo, B.; Thakur, A. Recent advances on synthesis, characterization and high frequency applications of Ni-Zn ferrite nanoparticles. *J. Magn. Magn. Mater.* **2021**, *530*, 167925. [CrossRef]
51. Shahane, G.S.; Kumar, A.; Arora, M.; Pant, R.P.; Lal, K. Synthesis and characterization of Ni–Zn ferrite nanoparticles. *J. Magn. Magn. Mater.* **2010**, *322*, 1015–1019. [CrossRef]
52. Gajbhiye, N.S.; Prasad, S. Thermal decomposition of hexahydrated nickel iron citrate. *Thermochim. Acta* **1996**, *285*, 325–336. [CrossRef]
53. Zhang, C.-Y.; Shen, X.-Q.; Zhou, J.-X.; Jing, M.-X.; Cao, K. Preparation of spinel ferrite $NiFe_2O_4$ fibres by organic gel-thermal decomposition process. *J. Sol-Gel Sci. Technol.* **2007**, *42*, 95–100. [CrossRef]
54. Itoh, H.; Takeda, T.; Naka, S. Preparation of nickel and Ni-Zn ferrite films by thermal decomposition of metal acetylacetonates. *J. Mater. Sci.* **1986**, *21*, 3677–3680. [CrossRef]
55. Hwang, J.; Choi, M.; Shin, H.-S.; Ju, B.-K.; Chun, M. Structural and Magnetic Properties of NiZn Ferrite Nanoparticles Synthesized by a Thermal Decomposition Method. *Appl. Sci.* **2020**, *10*, 6279. [CrossRef]
56. Itoh, H.; Uemura, T.; Yamaguchi, H.; Naka, S. Chemical vapour deposition of epitaxial Ni-Zn ferrite films by thermal decomposition of acetylacetonato complexes. *J. Mater. Sci.* **1989**, *24*, 3549–3552. [CrossRef]
57. Stoia, M.; Barvinschi, P.; Tudoran, L.B.; Barbu, M.; Stefanescu, M. Synthesis of nanocrystalline nickel ferrite by thermal decomposition of organic precursors. *J. Therm. Anal. Calorim.* **2012**, *108*, 1033–1039. [CrossRef]
58. Jeremić, D.; Andjelković, L.; Milenković, M.R.; Šuljagić, M.; Ristović, M.Š.; Ostojić, S.; Nikolić, A.S.; Vulić, P.; Brčeski, I.; Pavlović, V. One-pot combustion synthesis of nickel oxide and hematite: From simple coordination compounds to high purity metal oxide nanoparticles. *Sci. Sinter.* **2020**, *52*, 481–490. [CrossRef]
59. Iacob, M.; Racles, C.; Tugui, C.; Stiubianu, G.; Bele, A.; Sacarescu, L.; Timpu, D.; Cazacu, M. From iron coordination compounds to metal oxide nanoparticles. *Beilstein J. Nanotechnol.* **2016**, *7*, 2074–2087. [CrossRef]
60. Jesus, J.C.D.; González, I.; Quevedo, A.; Puerta, T. Thermal decomposition of nickel acetate tetrahydrate: An integrated study by TGA, QMS and XPS techniques. *J. Mol. Catal. A Chem.* **2005**, *228*, 283–291. [CrossRef]
61. Kumar, N.; Kachroo, P.L.; Kant, R. Thermal decomposition of some N-oxide complexes of cobalt(II), nickel(II) and copper(II) carboxylates. *J. Therm. Anal.* **1979**, *17*, 81–85. [CrossRef]
62. Dollimore, D.; Pearce, J. Changes in the surface characteristics of residues from the thermal decomposition of nickel oxysalts. *J. Therm. Anal.* **1974**, *6*, 321–333. [CrossRef]
63. Sun, Z.-L. Characteristics of thermal decomposition products of rare earth, alkali earth metal and transition metal p toluenesulfonates. *J. Therm. Anal. Calorim.* **2005**, *79*, 731–735. [CrossRef]
64. García, A.R.; Laverat, A.G.; Prudencio, C.V.R.; Méndez, A.J. Synthesis and thermal decomposition of Co(II), Ni(II), Cu(II), Zn(II), Cd(II), and Pb(II) m-benzenedisulphonates. *Thermochim. Acta* **1993**, *213*, 199–210. [CrossRef]
65. Fereshteh, Z.; Salavati-Niasari, M. Effect of ligand on particle size and morphology of nanostructures synthesized by thermal decomposition of coordination compounds. *Adv. Colloid Interface Sci.* **2017**, *243*, 86–104. [CrossRef]
66. Šuljagić, M.; Vulić, P.; Jeremić, D.; Pavlović, V.; Filipović, S.; Kilanski, L.; Lewinska, S.; Slawska-Waniewska, A.; Milenković, M.R.; Nikolić, A.S.; et al. The influence of the starch coating on the magnetic properties of nanosized cobalt ferrites obtained by different synthetic methods. *Mater. Res. Bull.* **2021**, *134*, 111117. [CrossRef]
67. Andjelković, L.; Jeremić, D.; Milenković, M.R.; Radosavljević, J.; Vulić, P.; Pavlović, V.; Manojlović, D.; Nikolić, A.S. Synthesis, characterization and in vitro evaluation of divalent ion release from stable $NiFe_2O_4$, $ZnFe_2O_4$ and core-shell $ZnFe_2O_4$@$NiFe_2O_4$ nanoparticles. *Ceram. Int.* **2020**, *46*, 3528–3533. [CrossRef]
68. Kilanski, L.; Lewinska, S.; Slawska-Waniewska, A.; Pavlović, V.B.; Filipović, S. Attempts to obtain $BaTiO_3/Fe_2O_3$ core-shell type structures: The role of iron oxide nanoparticle formation and agglomeration. *Inorg. Chem. Commun.* **2022**, 145. [CrossRef]
69. Syazwan, M.M.; Hapishah, A.N.; Azis, R.S.; Abbas, Z.; Hamidon, M.N. Grain growth effects on magnetic properties of $Ni_{0.6}Zn_{0.4}Fe_2O_4$ material prepared using mechanically alloyed nanoparticles. *Results Phys.* **2018**, *9*, 842–850. [CrossRef]
70. Ranga Mohan, G.; Ravinder, D.; Ramana Reddy, A.V.; Boyanov, B.S. Dielectric properties of polycrystalline mixed nickel–zinc ferrites. *Mater. Lett.* **1999**, *40*, 39–45. [CrossRef]
71. Singh, S.; Kumar, N.; Bhargava, R.; Sahni, M.; Sung, K.; Jung, J.H. Magnetodielectric effect in $BaTiO_3/ZnFe_2O_4$ core/shell nanoparticles. *J. Alloys Compd.* **2014**, *587*, 437–441. [CrossRef]

72. Yu, Z.; Ang, C. Maxwell–Wagner polarization in ceramic composites $BaTiO_3$–$(Ni_{0.3}Zn_{0.7})Fe_{2.1}O_4$. *J. Appl. Phys.* **2001**, *91*, 794–797. [CrossRef]
73. Bammannavar, B.K.; Naik, L.R. Electrical properties and magnetoelectric effect in (x)$Ni_{0.5}Zn_{0.5}Fe_2O_4$+(1−x)BPZT composites. *Smart Mater. Struct.* **2009**, *18*, 85013. [CrossRef]
74. Curecheriu, L.P.; Buscaglia, M.T.; Buscaglia, V.; Mitoseriu, L.; Postolache, P.; Ianculescu, A.; Nanni, P. Functional properties of $BaTiO_3$–$Ni_{0.5}Zn_{0.5}Fe_2O_4$ magnetoelectric ceramics prepared from powders with core-shell structure. *J. Appl. Phys.* **2010**, *107*, 104106. [CrossRef]
75. Macdonald, J.R. *Impedance Spectroscopy: Emphasizing Solid Materials and Systems*; Wiley: Hoboken, NY, USA, 1987.
76. Nuzhnyy, D.; Bovtun, V.; Savinov, M.; Kempa, M.; Petzelt, J.; Kaman, O.; Klementová, M.; Kuličková, J.; Jirák, Z. Synthesis and broadband dielectric-infrared spectroscopy of $La_{1-x}Sr_xMnO_3$@$BaTiO_3$ nanocomposite. *Mater. Res. Bull.* **2021**, *144*, 111459. [CrossRef]
77. Petzelt, J.; Nuzhnyy, D.; Bovtun, V.; Savinov, M.; Kempa, M.; Rychetsky, I. Broadband dielectric and conductivity spectroscopy of inhomogeneous and composite conductors. *Phys. Status Solidi Appl. Mater. Sci.* **2013**, *210*, 2259–2271. [CrossRef]
78. Jonscher, A.K. A new understanding of the dielectric relaxation of solids. *J. Mater. Sci.* **1981**, *16*, 2037–2060. [CrossRef]
79. Dzunuzovic, A.S.; Petrovic, M.M.V.; Bobic, J.D.; Ilic, N.I.; Stojanovic, B.D. Influence of ferrite phase on electrical properties of the barium zirconium titanate based multiferroic composites. *J. Electroceramics* **2021**, *46*, 57–71. [CrossRef]
80. Lee, J.Y.; Lai, B.C. Chapter 1—The electrical properties of high-dielectric-constant and ferroelectric thin films for very large scale integration circuits. In *Handbook of Thin Films*; Singh Nalwa, H., Ed.; Academic Press: Burlington, VT, USA, 2002; pp. 1–98. ISBN 978-0-12-512908-4.
81. Kundu, T.K.; Lee, J.Y. Thickness-Dependent Electrical Properties of $Pb(Zr,Ti)O_3$ Thin Film Capacitors for Memory Device Applications. *J. Electrochem. Soc.* **2000**, *147*, 326. [CrossRef]
82. Andjelković, L.; Šuljagić, M.; Lakić, M.; Jeremić, D.; Vulić, P.; Nikolić, A.S. A study of the structural and morphological properties of Ni–ferrite, Zn–ferrite and Ni–Zn–ferrites functionalized with starch. *Ceram. Int.* **2018**, *44*, 14163–14168. [CrossRef]